FULL PAPER

Photocatalysis

ADVANCED
ENERGY
MATERIALS

www.advenergymat.de

Ordered Mesoporous TiO$_2$ Gyroids: Effects of Pore Architecture and Nb-Doping on Photocatalytic Hydrogen Evolution under UV and Visible Irradiation

Tobias Sebastian Dörr, Leonie Deilmann, Greta Haselmann, Alexey Cherevan, Peng Zhang, Peter Blaha, Peter William de Oliveira, Tobias Kraus, and Dominik Eder*

Pure and Nb-doped TiO$_2$ photocatalysts with highly ordered alternating gyroid architecture and well-controllable mesopore size of 15 nm via co-assembly of a poly(isoprene)-*block*-poly(styrene)-*block*-poly(ethylene oxide) block copolymer are synthesized. A combined effort by electron microscopy, X-ray scattering, photoluminescence, X-ray photoelectron spectroscopy, Raman spectroscopy, and density functional theory simulations reveals that the addition of small amounts of Nb results in the substitution of Ti^{4+} with isolated Nb^{5+} species that introduces inter-bandgap states, while at high concentrations, Nb prefers to cluster forming shallow trap states within the conduction band minimum of TiO$_2$. The gyroidal photocatalysts are remarkably active toward hydrogen evolution under UV and visible light due to the open 3D network, where large mesopores ensure efficient pore diffusion and high photon harvesting. The gyroids yield unprecedented high evolution rates beyond 1000 µmol h^{-1} (per 10 mg catalyst), outperforming even the benchmark P25-TiO$_2$ more than fivefold. Under UV light, the Nb-doping reduces the activity due to the introduction of charge recombination centers, while the activity in the visible triple upon incorporation is owed to a more efficient absorption due to inter-bandgap states. This unique pore architecture may further offer hitherto undiscovered optical benefits to photocatalysis, related to chiral and metamaterial-like behavior, which will stimulate further studies focusing on novel light–matter interactions.

1. Introduction

Hydrogen is considered as the green energy source of the future. One of the most promising routes to obtain this resource is the photoassisted production from water using solar energy.[1] Typically, a semiconductor material with a suitable bandgap (E_G), such as the most thoroughly studied titanium dioxide (TiO$_2$), converts photon energy into an electron–hole pair (i.e., exciton), which, after separation, migrates to the materials surface, eventually splitting water to O$_2$ and H$_2$.[1b,2] Despite considerable advances in recent research on photocatalysis, efforts remain devoted toward designing efficient catalysts capable of operating under solar light with high quantum efficiency, stability, durability, nontoxicity, and low cost.[3] Therefore, the community explores a wide range of materials design concepts.[4] One popular approach to improve the catalytic activity is to nanostructure the catalyst to achieve large surface areas, extended porosity, and, ideally, to control the exposed crystalline facets.[5] Typically, nanostructured materials come in a wide range of shapes and morphologies, such as quantum dots,[6] tubes,[7] rods,[8] sheets,[9] and wires.[10] Those nanoparticulate systems, however, often experience agglomeration/aggregation in liquid environments, consequently limiting reactant access to their active surface area (typically measured by Brunnauer–Emmett–Teller (BET) or density functional theory (DFT)).[11] This limits their validity as model systems in heterogeneous liquid catalysis.

Ordered porous catalysts have recently emerged as promising model catalysts and electrodes, due to their homogeneous pore distribution and tunable pore sizes.[12] A common approach is based on block copolymers (BCPs) as structure-directing agents using an evaporation-induced self-assembly (EISA) process.[13] Most researchers have used commercial polymers (e.g., Pluronic), which typically yield 2D pore arrangements with pore diameters below 10 nm.[14] However, recent advances have demonstrated that such small pores are not sufficiently large to eliminate kinetic limitations imposed by reaction diffusion through the pores in liquid environments.[12e,15] Moreover, we could recently show that a 3D-interconnected pore network (such as alternating or double gyroids) greatly facilitates reactant diffusion and can thus provide ready access to the entire interior surface, consequently enhancing the

T. S. Dörr, Dr. P. Zhang, Dr. P. W. de Oliveira, Prof. T. Kraus
INM-Leibniz Institut für Neue Materialien
Campus D2 2, 66123 Saarbrücken, Germany
L. Deilmann, G. Haselmann, Dr. A. Cherevan, Prof. P. Blaha, Prof. D. Eder
Technische Universität Wien
Getreidemarkt 9, 1060 Wien, Austria
E-mail: dominik.eder@tuwien.ac.at

photocatalytic performance to a large extent.[16] For example, we demonstrated for photocatalytic hydrogen evolution that ordered mesoporous CsTaWO₆ catalysts with 40 nm pore sizes and a gyroidal architecture greatly outperformed those derived from the commercial Pluronic P-123 with 1D pores and 5 nm pore diameters.[14b,17]

The synthesis of ordered mesoporous metal oxide networks using BCP directed coassembly with a metal organic precursor through evaporation induced self-assembly has been pioneered by Wiesner and co-workers[18] and Stucky and co-workers[19] for silica (SiO₂) and aluminosilicates. TiO₂ was the first ordered mesoporous transition metal oxide and primarily synthesized for use in dye-sensitized solar cells (DSSCs).[20] In contrast to, for instance, tantalum oxide (Ta₂O₅), where extended crystalline domains have been reported (>25 nm),[21] mesoporous anatase TiO₂ typically comprises of distinctly smaller crystallites (≈10 ± 5 nm) within the walls.[22] This compartmentalization is highly interesting, considering that the materials resistivity, and thus charge mobility, notably depends on the crystalline nature (i.e., size, topology, degree).[23] In photocatalysis, small crystallites can offer short diffusion ways for the excitons and lower recombination rates due to charge transfer in-between the grains.

Another approach toward advancing photocatalysts involves the tuning of the bandgap,[24] which has often been attempted via substitutional doping to prepare visible light photon harvesting catalysts.[1b,25] An example is the substitution on the Ti^{4+} sites by Nb^{5+} at low oxygen activity which includes the formation of Ti^{3+} defect states within the original bandgap of TiO₂ near its conduction band minimum (CBM).[26] This typically gives rise to an extended absorption range (e.g., bluish samples) and thus allows solar driven catalysis. Yet, it also lowers the redox potential of the separated excitons and, crucially, favors the formation of recombination centers, which considerably reduces the catalyst's activity.[1b,27] As a result, the activity of catalysts with visible light response often suffers under UV irradiation. In contrast, oxygen-rich environments upon synthesis are expected to favor the formation of Ti^{4+} vacancies and O^{2-} interstitials (O''_i), thus reducing the aforementioned limitations.[27] However, prediction of the materials response to light and its activity is not easy, in particular since the amount of doping significantly affects the electronic structure, crystallinity, and even morphology of the catalyst.[28]

In this work, we designed a model system comprising of pure and Nb-doped TiO₂ catalysts with a highly ordered mesoporous network of alternating gyroids and uniform pore diameters of 15 nm, via modified co-assembly of metal–organic precursors and an optimized poly(isoprene)-*block*-poly(styrene)-*block*-poly(ethylene oxide) (ISO) BCP (Section 2.1). The samples were characterized with a wide range of techniques, including X-ray powder diffraction (XRD), small-angle X-ray scattering (SAXS), X-ray photoelectron spectroscopy (XPS), transmission electron microscopy (TEM), energy-dispersive X-ray spectroscopy (EDX), diffuse reflectance spectroscopy (DRS), photoluminescence (PL), Raman spectroscopy, and inductively coupled plasma optical emission spectrometry (ICP-OES) toward their phase composition (Section 2.2) and morphology (Section 2.3) that is further supported by computational simulations using density functional theory. A crucial difference of lattice incorporation for Nb-doping has been found: small amounts of Nb resulted in preferential anisotropic incorporation, while lager amounts of Nb led to spatial clustering (Section 2.4). Finally, we evaluated and compared the photocatalytic performance of the samples toward hydrogen evolution under both, UV and visible illumination, benchmarked against similarly prepared nanoparticle (NP) references and a commercial P25-TiO₂ (Section 2.5).

2. Results and Discussions

2.1. Synthesis of Mesoporous Catalysts

The synthesis route for ordered mesoporous alternating gyroidal (G^A) TiO₂ is based on a macromolecular coassembly process and summarized in **Figure 1**. We first prepared an ISO terpolymer by sequential anionic polymerization, comprising of 30, 60, and 10 vol% of poly(isoprene) (PI), poly(styrene) (PS), and poly(ethylene oxide) (PEO), respectively, with a molecular weight (M_W) of 61 000 g mol⁻¹ and a narrow polydispersity (D_P) of 1.09. The ISO was dissolved in tetrahydrofuran (THF) and mixed with a precursor solution containing either pure Ti(^{i}Prop)₄ or a mixture of Ti(^{i}Prop)₄ and Nb(OEt)₅, which selectively swelled the PEO block. The final structure of the catalyst material was defined by the relative volume fractions of the
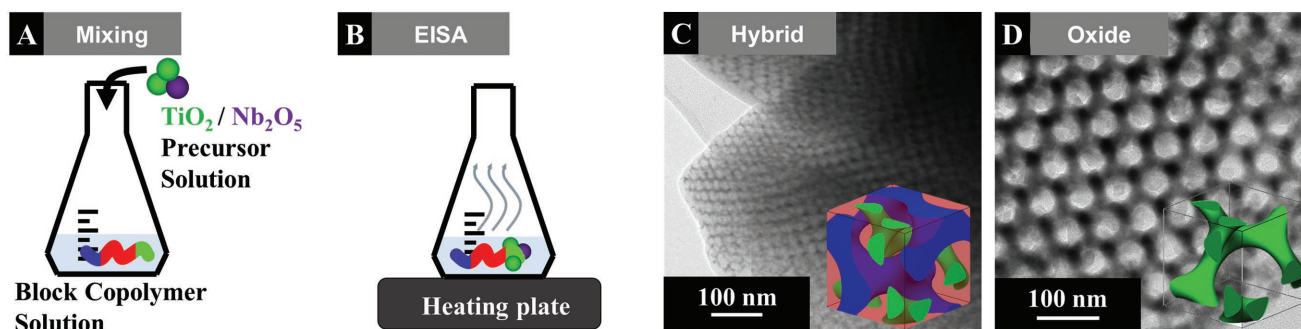

Figure 1. Illustration of the evaporation-induced self-assembly (EISA) based on the preparation of ordered mesoporous pure and Nb-doped TiO₂. A) A solution of the block copolymer is mixed with an adjusted amount of a precursor containing solution. B) Evaporation of the solvent induces self-assembly of the polymer, while the inorganic precursor selectively swells the PEO block. C) TEM image of the resulting polymer–inorganic hybrid with the expected arrangement (schematics in inset) before calcination and D) TEM image of the freestanding porous oxide after calcination with the expected gyroidal architecture (schematics in inset).

polymer blocks after swelling and optimized by adjusting the ISO composition and amount of precursor solution.[29] The solutions were subjected to an EISA process to achieve gyroidal polymer–inorganic assemblies (further named as ISO/G^A-TiO2, ISO/G^A-TNO1, and ISO/G^A-TNO3). These solid hybrids were then calcined at 400 °C to remove the polymer and crystallize the inorganic gels to yield the respective porous gyroidal metal oxides, that is, the pure titania (sample: G^A-TiO2), and the 1 or 3 at% Nb-doped titania (sample: G^A-TNO1 and G^A-TNO3, respectively).

2.2. Phase Composition

XRD (**Figure 2**A) revealed that all calcined samples consisted nearly exclusively of the anatase phase (PDF No. 03-065-5714). This corresponds well with literature, where it is known that low process temperatures typically form the kinetically favored anatase rather than thermodynamic-stable rutile.[30] Yet, structural refinement showed that the pure TiO_2 sample contained a tiny amount (i.e., 3.2 mass%) of rutile. The amount decreased to 1.7 mass% upon doping, independent of the Nb concentration (Table S1, Supporting Information). It is further important to highlight the absence of any impurity phases, such as niobium oxides or mixed oxide solutions.

This is in line with Raman spectroscopy (Figure 2B), where all samples showed the typical modes associated with the anatase phase: a sharp $E_g(1)$ mode at 144 cm^{-1}, the characteristic $E_g(2)$ (196 cm^{-1}), B_{1g} (394 cm^{-1}), $E_g(3)$ (636 cm^{-1}) bands, and the combined B_{1g}/A_{1g} mode (centered at 514 cm^{-1}).[31] Any possible rutile modes were likely below the detection limit. Also, we did not observe any impurity phases (e.g., Nb_2O_5), in line with XRD. The incorporation of Nb slightly broadened the B_{1g} mode and caused a tiny shift toward lower Raman shift, which is consistent with previous works.[32] The center of the most intense $E_g(1)$ mode shifted from 144 to 146 cm^{-1} with increased Nb content.

Importantly, we did not observe any residual carbon in the calcined samples. This was in line with the thermogravimetric analysis (TGA, Figure S1A, Supporting Information) data of solid hybrids without calcination, which revealed the typical weight losses, induced by residual solvent evaporation (below 200 °C), the combustion of the precursor ligands (250–330 °C), and the oxidation of the polymer (above 350 °C). Crucially, when holding the calcination temperature at 400 °C for 4 h to simulate the calcination conditions for our sample, no additional weight loss was detected, hence confirming complete polymer removal. In addition, we did not observe any sp^2/sp^3 carbon-related peaks in Raman spectroscopy up to 2500 cm^{-1} (Figure S1B, Supporting Information).[16] This is in line with TEM, which shows no carbon layer on the materials' surfaces (**Figure 3**D–I). The absence of carbon in other forms can also be excluded by ICP-OES (Table S2, Supporting Information). All results thus confirm the complete removal of the structure-directing polymer upon calcination.
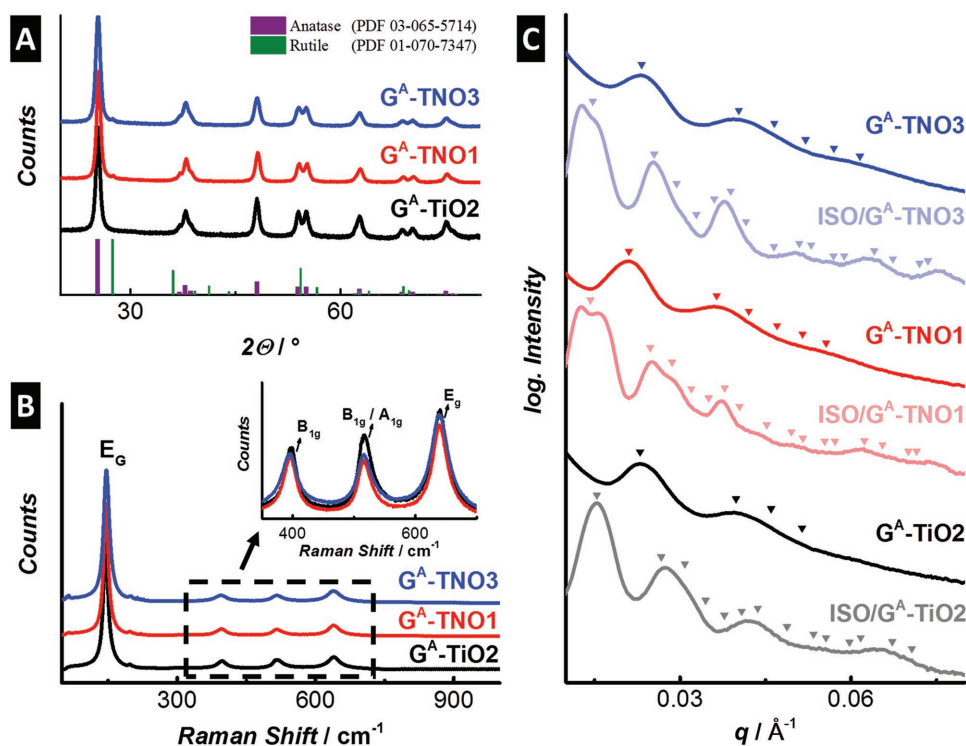

Figure 2. A) X-ray diffraction data for G^A-TiO2, G^A-TNO1, and G^A-TNO3, respectively, with reference data for anatase and rutile TiO_2 crystalline peaks marked in the curve. B) Raman spectra for the three samples with B_{1g}, B_{1g}/A_{1g}, and E_g peaks shown in the inset. C) Small-angle X-ray scattering data of the ISO/precursor hybrids and calcined samples. The theoretically predicted scattering positions corresponding to an alternating gyroid (G^A) structure are marked with triangles. For clarity reasons, the curves are shifted proportionally along the y-axis. The first peak center is set as $q*$.

**ADVANCED
SCIENCE NEWS**
www.advancedsciencenews.com
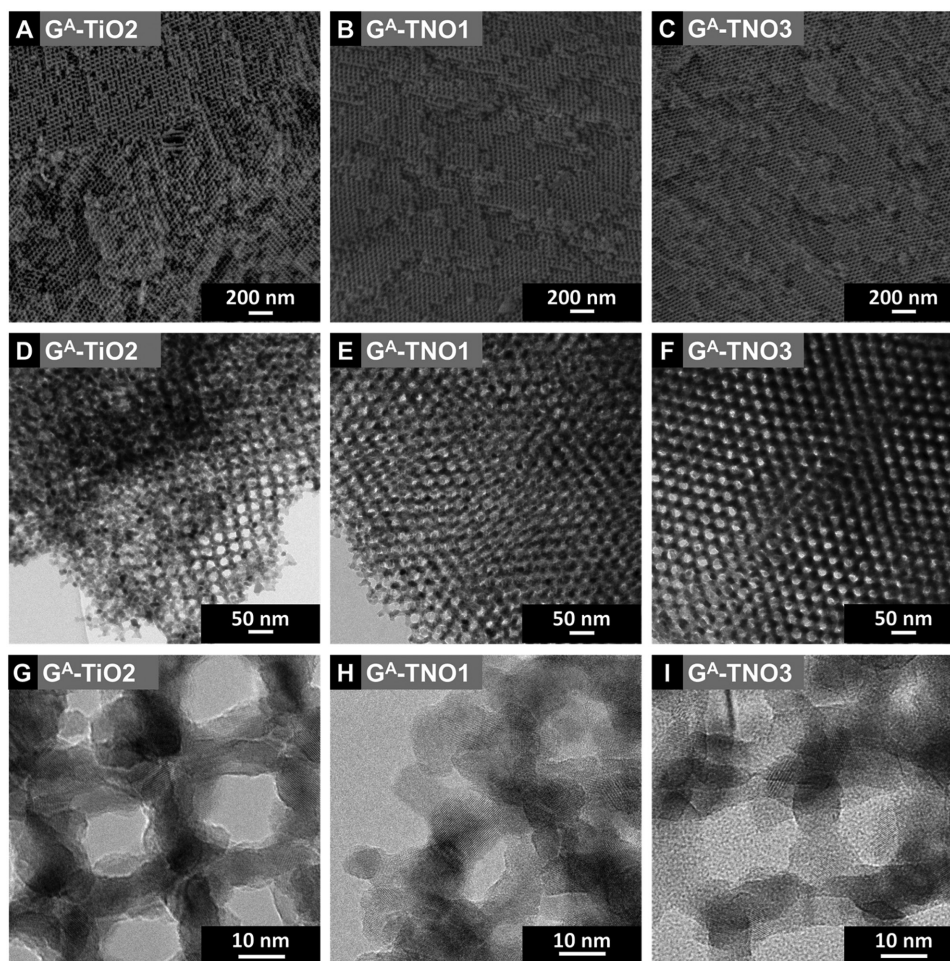
**ADVANCED
ENERGY
MATERIALS**
www.advenergymat.de

Figure 3. A–C) Scanning electron microscopy images and D–F) low- and G–I) high-magnification transmission electron microscopy images of the calcined G^A-TiO2, G^A-TNO1, and G^A-TNO3.

2.3. Pore Structure

Scanning electron microscopy (SEM) and TEM (Figure 3) data revealed that all calcined samples consisted of well-ordered mesopores with remarkably uniform pore diameters of around 15 nm. There was no noteworthy effect of the introduction of Nb on the pore architecture or pore diameter. The walls of the pores were composed of randomly oriented nanocrystals of around 10 nm, as estimated from TEM in Figure 3G–I.[22] Again, the addition of Nb did not significantly alter the compartmentalization of the pore walls or the size of the nanocrystals.

The porosity of the samples was investigated by nitrogen physisorption (BET, Figure S1C, Supporting Information). All nitrogen isotherms were largely identical in shape and show type IVa hysteresis, which is typical for a mesoporous material.[33] The specific surface areas (SSA_{BET}) were measured as 82, 95, and 100 m^2 g^{-1} for G^A-TiO2, G^A-TNO1, and G^A-TNO3, respectively, and the total pore volume was calculated to be 0.81 cm^3 g^{-1} (G^A-TiO2), 0.84 cm^3 g^{-1} (G^A-TNO1), and 0.89 cm^3 g^{-1} (G^A-TNO3).

SAXS provided in-depth information on the pore ordering, derived from the first scattering peak ($q*$) and the respective ratios with the higher order peaks (q). Figure 2C reveals a clear periodicity in ISO/G^A-TiO2, with the calculated $q/q*$ ratios correlating well with the theoretical scattering pattern of a typical alternating gyroid (G^A) morphology ($q/q* = 1$, $\sqrt{3}$, $\sqrt{4}$, $\sqrt{5}$,...).[34] Crucially, the G^A structure was largely preserved upon calcination, which is in line with the aforementioned SEM/TEM results. Note that the domain real-space spacing (d), calculated by $d = 2\pi q^{-1}$ had decreased from 41 to 27 nm, corresponding to a decrease of 32%, as indicated by the shift of $q*$ toward higher q-values.[12c] This is attributed to shrinkage of the Ti-containing domains upon calcination. Both, G^A-TNO1 and G^A-TNO3, show a comparable gyroid structure and a similar shrinkage extent of around 35%. Interestingly, we observed a significant split in the first scattering peak, which is indicative of structural complexity, as seen in the nonsymmetric 2D radial scattering for $q*$ (Figure S2, Supporting Information).

2.4. Incorporation of Niobium

The respective amounts of Nb in the samples were quantified by ICP-OES (Table S2, Supporting Information) and agreed well
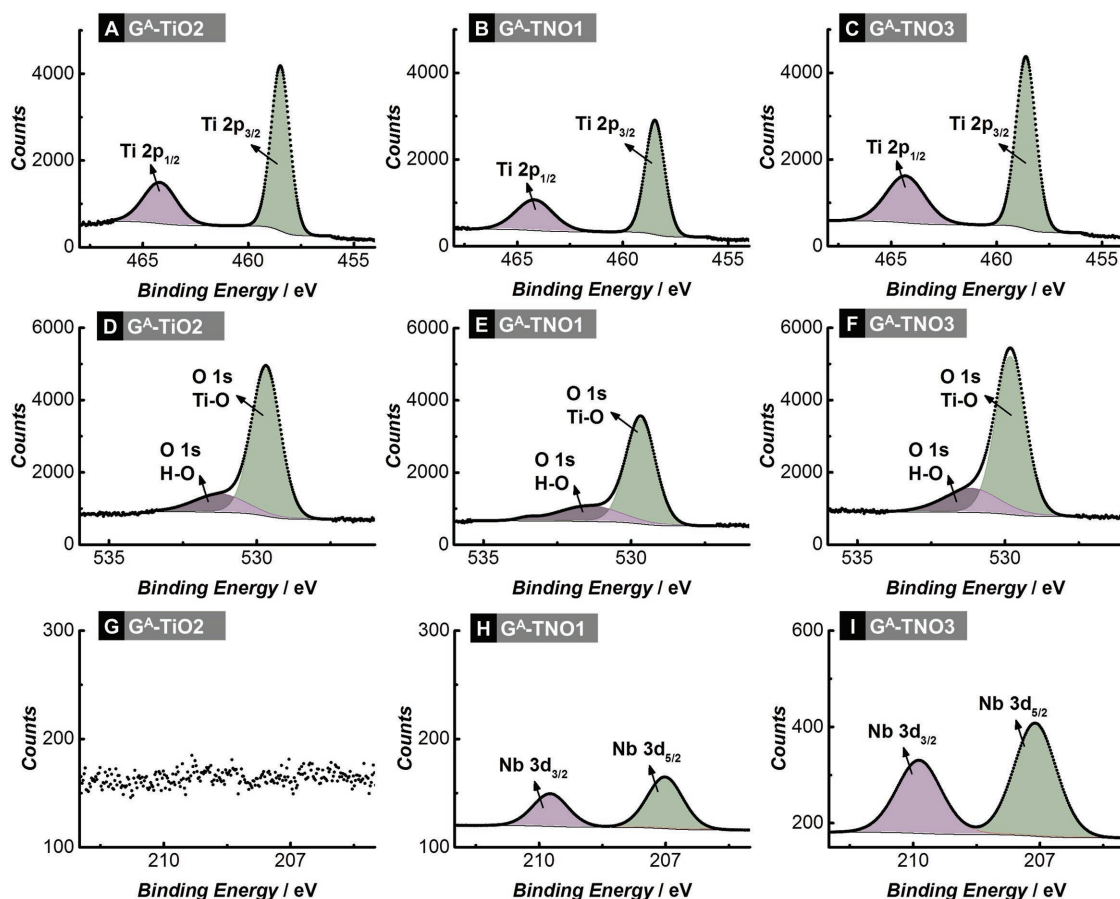
Figure 4. X-ray photoelectron spectroscopy data: A–C) Ti 2p spectra, D,E) O 1s spectra, and G–I) Nb 3d spectra of G^A-TiO2, G^A-TNO1, and G^A-TNO3, respectively.

with the expected values of 1.15 and 2.78 at%, for G^A-TNO1 and G^A-TNO3, respectively. A qualitative distribution can be derived from TEM-EDX analysis of the structured doped samples (Figure S3, Supporting Information). Rietfeld analysis of the XRD pattern revealed that the unit cells in both Nb-containing samples were larger than in the pure TiO_2, which suggests a substitutional doping of Ti with Nb (Table S1, Supporting Information). It is intriguing, however, that the expansion of the unit cell in G^A-TNO1 along the c-direction was considerably more pronounced (increase of c by 0.006 Å) than in a, b-direction (no apparent increase). This contrasts with G^A-TNO3, which showed a purely isotropic lattice widening.

The surprising anisotropic lattice increase in G^A-TNO1 was investigated further by DFT based simulations. Since DFT calculations do not have the accuracy to calculate lattice parameters on an absolute scale with the required precision, we quantified the changes of the nearest-neighbor Nb−O and Nb−Ti distances along the z (equals c) or x,y (equals a,b) directions when we relaxed the atomic positions until the forces were below 1 mRy bohr^{-1}. We found that the six nearest neighbor O atoms relaxed on average by 0.015 Å away from Nb, but there was marked anisotropy, and the largest increase of 0.020 Å was found in the z-direction. Similarly, the four nearest Ti atoms (which are above/below the x,y-plane) relaxed by 0.05 Å, while the four next nearest neighbors (all in the same x,y-plane)

increased their distance only by 0.03 Å. This is in accord with the measured 0.006 Å larger c lattice parameter of Nb-doped anatase and confirms an anisotropic substitutional doping.

XPS was used to analyze the oxidation state of the dopant and to clarify the nature of charge compensation, shown in **Figure 4**. It is important to note that all samples exclusively showed Ti^{4+} in the Ti 2p photoemission spectrum independent of doping.[35] A typical oxide splitting value of 5.7 eV between Ti 2p$_{1/2}$ and Ti 2p$_{3/2}$ was found. Although the full-width at half maximum (FWHM) for each spin–orbital component is expected to be the same, in the case of Ti 2p, the Ti 2p$_{1/2}$ is much more short living, broadened, and less distinct than expected (Coster–Kronig effect).[36] The O 1s spectrum was similar over all samples with no noticeable effect of material doping. Typical binding values for lattice oxygen (green, 529 eV) were found, but they tended to broaden toward higher binding energies (BEs) due to hydroxide surface groups (violet, centered ≈531 eV). In contrast, the Nb 3d spectra differed strongly between the pure and doped samples. As expected, no Nb was found for G^A-TiO2, while both, G^A-TNO1 and G^A-TNO3, contained the characteristic Nb 3d$_{5/2}$ and Nb 3d$_{3/2}$ peaks with their intensity increasing with higher Nb content. The Nb 3d signal splits in a ratio of 2:3 with 2.78 eV and symmetric FWHM (Table S3, Supporting Information), in line with literature.[37] However, G^A-TNO3 showed a significant decrease in binding
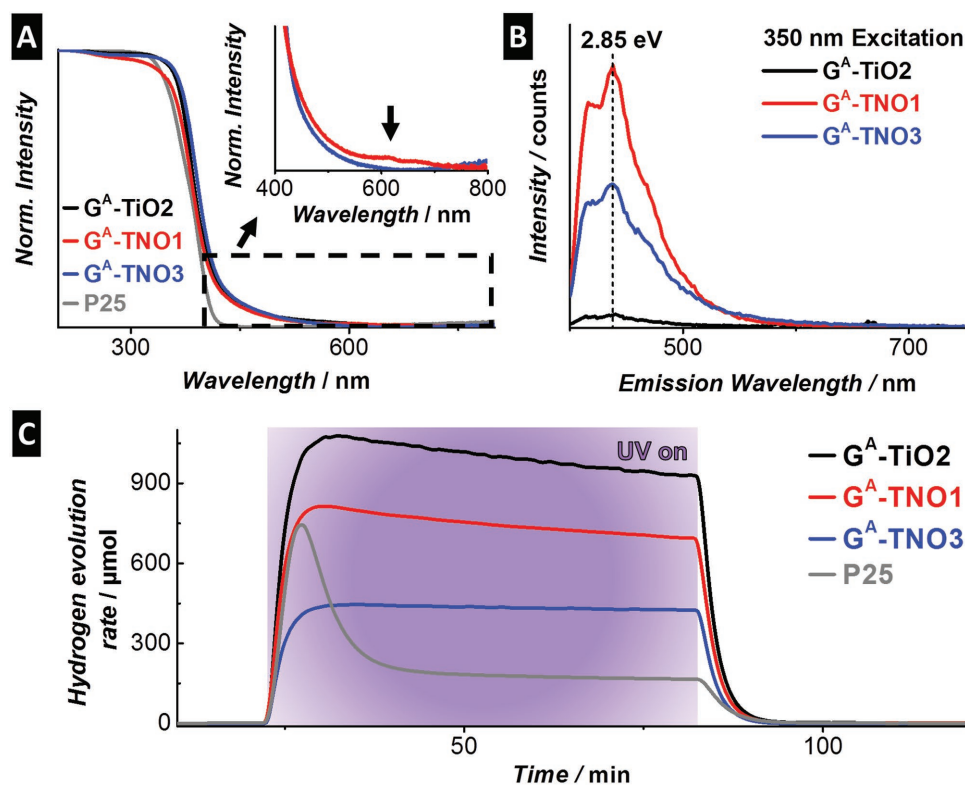
Figure 5. A) Diffuse reflectance spectroscopy of gyroidal samples and the commercial P25 reference with magnification of visible light range (400–800 nm). B) Photoluminescence spectra for gyroidal samples, excited with 350 nm laser. C) Evolution profiles of UV-driven hydrogen evolution ($\lambda = 240$–400 nm) for G^A-TiO2, G^A-TNO1, G^A-TNO3, and the commercial P25 reference.

energy of the Nb 3d by around 0.7 eV with respect to an identically prepared gyroidal Nb_2O_5 reference (Table S3, Supporting Information). A lower binding energy corresponds to a lower oxidation state of Nb due to a higher local electron density, such as provided by interstitial O''_i species, which may be present to charge compensate for Nb^{5+} doping.[38]

The presence of Nb is expected to affect the optical properties of TiO_2,[27] which we investigated with DRS (**Figure 5**A) as well as solid-state PL (Figure 5B). The absorption edge was almost identical for all gyroidal samples; the bandgap was calculated as 3.0 eV, which is in line with literature.[39] The absence of an extended absorption feature below 500 nm confirms that no Ti^{3+} defect states were formed within the TiO_2 bandgap, in line with XPS results.[40] Interestingly, G^A-TNO1 additionally exhibited weak absorption peaks at around 600 nm, which can be assigned to discrete intra-bandgap states formed by Nb within the minority rutile phase.[26d] The absence of this absorption features in G^A-TNO3 may well be explained by the tendency of Nb to form clusters, which instead favors the formation of shallow trap states within the TiO_2 CBM.[28] This hypothesis was tested by DFT simulations. Indeed, it appears that at higher Nb contents, the tendency of Nb atoms to cluster around the additional interstitial O''_i atom (i.e., when two Nb atoms are direct neighbors of the O-interstitial) is energetically more favorable by about 0.4 eV than the formation of isolated sites (i.e., when one Nb is close, but the other one is as far away as possible).

The doping and its effect on charge carrier trapping and transfer was further analyzed by PL with 350 nm excitation

(Figure 5b). The observed weak photoluminescence of G^A-TiO2 is in line with literature and has been attributed to a reduced recombination rate due to mobile charge carriers, charge transfer, or radiative quenching by surface groups.[41] Due to the high oxygen activity upon material's synthesis, we cannot exclude additional O''_i species as origin of the PL response, yet, only small amounts might be present as stabilizing higher valent metal atoms are not present in pure G^A-TiO2. However, the addition of Nb has significantly increased these defects causing a stronger emission response. In contrast, the Nb-containing samples showed a strong peak centered at around 440 nm (≈ 2.8 eV), with the highest photoluminescence intensity found for G^A-TNO1. Again, this can be explained by the presence of O''_i species, which may act as electron sinks and facilitate radiative recombination. Consequently, the more Nb species, the faster the recombination would be expected. However, in the case of G^A-TNO3, the comparative decrease in PL intensity can be attributed to the aforementioned Nb clustering, which favors non-radiative d-d transitions of the excited electrons within the shallow trap states.[26d,28,42]

In summary, the combined results from XPS, SAXS/XRD, DRS/PL/Raman spectroscopy, and DFT studies revealed several key features of our gyroidal photocatalysts. First, we found an absence of Ti^{3+}, which typically broadens the Ti 2p peaks in XPS toward lower binding energies.[43] Based on the downshift of the Nb 3d peak, we assume that the electron deficiency in our doped materials is charge compensated mainly by O^{2-} interstitials (O''_i), although a contribution by Ti^{4+} vacancies (V''''_{Ti}), as

**ADVANCED
SCIENCE NEWS**
www.advancedsciencenews.com

**ADVANCED
ENERGY
MATERIALS**
www.advenergymat.de

previously reported for high oxygen activity upon synthesis[26b–d] and polymer derived mesoporous materials,[44] is additionally possible. The results further suggest that, at low concentrations, Nb incorporates preferably as isolated species, introducing inter-bandgap states, while at higher concentrations, it prefers to cluster and form shallow states near the TiO_2 CBM. Both, the nature of Nb incorporation and charge compensation species, are expected to affect the photocatalytic performance of our catalysts.

2.5. Photocatalytic Evaluation

The photocatalytic performance of the samples was evaluated toward hydrogen evolution for both, UV (λ = 240–400 nm) and visible light (λ = 400–800 nm). As reference materials, we used (i) NPs, which were prepared under identical conditions as the gyroids, but without BCP (sample: NP-TiO2, NP-TNO1, and NP-TNO3 for the pure, 1 and 3 at% doped sample, respectively), and (ii) commercial P25-TiO₂ (sample: P25). The first references enabled us to investigate the influence of our 3D ordered mesoporous structure, while P25 allowed a setup-independent comparison with literature. Characterization of the reference materials can be found in Figure S4 (Supporting Information). For the photocatalytic test reaction a dispersion of 10 mg in a 1:1 H_2O:MeOH model solution was used with in situ photodeposited Pt as cocatalyst (≈0.5 mass%). The actual amount of Pt was 0.43 mass%, as quantitatively confirmed by post-mortem ICP-OES (Table S2, Supporting Information). The particles were of uniform size (≈2 nm) and well distributed on the surface of the catalysts (the visual representation of the Pt NPs with TEM can be found in Figure S5, Supporting Information).

2.5.1. UV Irradiation

The hydrogen evolution profiles are shown in Figure 5C, while the steady-state hydrogen evolution rates (HER) are summarized in **Figure 6**A. We observed three key features:

(1) Pore structure: The gyroids clearly outperformed the nanoparticulate counterparts to a large extent. For example, G^A-TiO2 and the corresponding NP-TiO2 showed activities of

1001 ± 76 µmol h⁻¹ (mass-correlated: 0.1 mol g⁻¹ h⁻¹) and 194 ± 7 µmol h⁻¹ (mass-correlated: 0.02 mol g⁻¹ h⁻¹), respectively. The effect was even more pronounced when comparing to P25, where the activity of G^A-TiO2 was increased by 5.5 times. The HER of G^A-TiO2 corresponds to a photonic efficiency of ≈12% (calculation can be found in the Supporting Information) and is currently among the highest values reported for pure TiO_2 photocatalysts (**Table 1**). The reasons for the superior activity of the gyroidal structures are manifold. The gyroidal samples exhibit larger specific surface areas than the nanoparticulate references, yet, this only accounts for a 60% increase of the rates, at maximum. Another contribution may arise from the large mesopores and the 3D open network, which allows direct access to the interior surface without kinetic limitations from pore diffusion. Furthermore, the size of the nanocrystals (around 10 nm) that build the walls of the gyroids is considered ideal to ensure short diffusion ways for the photoexcited charge carriers to the active surface sites, while permitting charge transfer in-between the grains thus lowering the recombination tendency.[22] At last, the excellent long-range ordering of the gyroidal pore structure may induce beneficial optical effects, possibly related to the reported negative refractive index (RI)[52] and metamaterial-like behavior[53] in gyroidal materials, whose impact on photoinduced energy conversation has yet to be investigated.

(2) Stability: The commercial P25 showed a steady-state activity of 173 ± 12 µmol h⁻¹, which is in line with literature under comparable process conditions and underlines the viability of our setup. Note that the initial activity for P25 was considerably higher but had dropped after minutes, leading to the values reported in literature. This recently discovered early-stage deactivation is supposed to originate from a complex interplay of UV-induced oxygen vacancies and the Pt cocatalyst active sites, which induces a change in reaction mechanism associated with CO formation.[54] Importantly, a calcination treatment prior to the reaction to anneal oxygen vacancies can minimize this deactivation process, thus highlighting the impact of defects. Crucially, our gyroidal samples did not show this early-stage deactivation, owing to the fact that they had already been exposed to high temperatures in oxygen-rich atmosphere during the template removal and crystallization. We further conducted cycling and duration experiments (up to 20 h), which revealed a slow deactivation process that is typically assigned
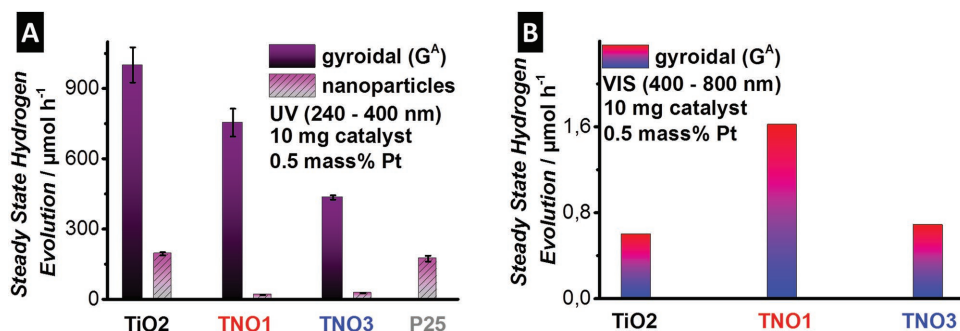
Figure 6. A) Steady-state evolution rates of UV-driven hydrogen evolution (λ = 240–400 nm) for G^A-TiO2, G^A-TNO1, G^A-TNO3, their nanoparticulate counterparts, and the commercial P25 reference. B) Steady-state evolution rates of visible-driven hydrogen evolution (λ = 400–800 nm) for G^A-TiO2, G^A-TNO1, G^A-TNO3; the values for the nanoparticle references (not shown) were below the detection limit.

Table 1. Exemplary results from UV-driven photocatalytic hydrogen evolution using pure TiO_2 taken from literature.

Crystal structure	Cocatalyst [mass%]	Setup		H_2 evolution rate		
		Light source	Reactant medium	Per hour (catalyst mass)	Mass-specific	Reference
Anatase	Pt (0.5)	Hg lamp 240–400 nm	H_2O:MeOH 1:1	1001 µmol h^{-1} (10 mg)	100.10 mmol h^{-1} g^{-1}	this work
Rutile	Pt (1)	Xe lamp 320–400 nm	H_2O:MeOH 9:1	2470 µmol h$^{-1a)}$ (100 mg)	24.70 mmol h^{-1} g^{-1}	[6a]
Anatase/rutile 67/33 mass%	Pt (0.5)	Xe lamp	H_2O:gylcerol 9:1	1026 µmol h^{-1} (100 mg)	10.26 mmol h^{-1} g$^{-1a)}$	[30]
Anatase	Pt (0.5)	Xe lamp 300–800 nm	H_2O:MeOH 22:5	405.2 µmol h^{-1} (60 mg)	6.75 mmol h^{-1} g$^{-1a)}$	[45]
Anatase/rutile	Pt (2.0)	LED 380 nm	H_2O:EtOH 1:1	385.0 µmol h^{-1} (50 mg)	7.70 mmol h^{-1} g$^{-1a)}$	[46]
Anatase/rutile 80/20 mass%	1:10 Ni:Pd (1) 10:1 Ni:Pd (0.5)	Hg lamp	H_2O:MeOH 1:1	≈220 µmol h^{-1} ≈130 µmol h^{-1} (50 mg)	4.40 mmol h^{-1} g$^{-1a)}$ 2.60 mmol h^{-1} g$^{-1a)}$	[47]
Anatase	Cu (1.5) Pd (1) Au (2)	Hg lamp	H_2O:MeOH 10:1	350 µmol h^{-1} 420 µmol h^{-1} 557 µmol h^{-1} (200 mg)	1.75 mmol h^{-1} g$^{-1a)}$ 2.10 mmol h^{-1} g$^{-1a)}$ 2.78 mmol h^{-1} g$^{-1a)}$	[48]
Anatase	Pt (0.2)	LED 365 nm	H_2O:MeOH 8:2	90.6 µmol h$^{-1a)}$ (50 mg)	1.81 mmol h^{-1} g$^{-1a)}$	[49]
Anatase	Rh (2) Pt (2)	Hg lamp 250–400 nm	Water vapor (10 mass% NaOH coated)	449 µmol h^{-1} 284 µmol h^{-1} (300 mg)	1.50 mmol h^{-1} g$^{-1a)}$ 0.95 mmol h^{-1} g$^{-1a)}$	[50]
Anatase	Pt (1)	Xe lamp 365 nm	H_2O:MeOH 8:2	68 µmol h^{-1} (100 mg)	0.68 mmol h^{-1} g$^{-1a)}$	[51]

$^{a)}$Calculated from given values.

to surface poisoning and active site blocking (Figure S6, Supporting Information).[55] Still, the overall performance of the gyroidal samples remained superior, even after 20 h.

(3) Nb-doping: The activity decreased considerably upon Nb incorporation, that is, from 755 ± 60 to 435 ± 9 µmol h^{-1} for G^A-TNO1 and G^A-TNO3, respectively. Similarly, the corresponding values for the nanoparticulate references decreased to 26 µmol h^{-1}. From PL we expect for both doped gyroidal samples an increased charge recombination rate by radiative relaxation compared to G^A-TiO2. The lower activity of G^A-TNO3 despite lower PL intensity is likely caused by d-d transition within the shallow trap states followed by nonradiative relaxation, for example, via thermalization.[26a]

2.5.2. Visible Irradiation

We tested our materials under visible light (400–800 nm) using the same experimental conditions as for UV-driven catalysis (Figure 6B). Not surprisingly, the nanoparticle references exhibited no detectable H_2 evolution, although DRS suggests a pronounced bathochromic shift. In contrast, the gyroids showed remarkably high activities of 0.60, 1.62, and 0.68 µmol h^{-1}, for G^A-TiO2, G^A-TNO1, and G^A-TNO3, respectively. Normalized to weight, these values amount to

60, 162, and 68 µmol h^{-1} g^{-1}, respectively. These high values demonstrate that the aforementioned characteristics of the gyroidal structure also dramatically benefit the performance under visible light that is also comparable to advanced state-of-the-art materials (selection is given within Table S5, Supporting Information).

In contrast to the UV-based results, the activities under visible increased with the incorporation of Nb. In fact, G^A-TNO1 exhibited an activity that was almost three times higher than of G^A-TiO2 and G^A-TNO3. We attribute this enhancement to the presence of isolates Nb species, whose intra-bandgap states can offer additional absorption sites for a more efficient light harvesting. In comparison, the decrease of HER in G^A-TNO3 is attributed to the formation of clusters and the charge compensation with oxygen interstitials, where shallow trap states within the TiO_2 CBM replace the intra-bandgap states, in line with DFT simulations. Finally, the anisotropic substitution of Nb may additionally affect the photocatalytic performance, which has yet to be investigated in more detail.

3. Conclusion

In this work, we report on the preparation of BCP-derived mesoporous pure and Nb-doped TiO_2 with alternating gyroid architecture. The pores were remarkably well-ordered and uniform in diameter (≈15 nm). All samples consisted mainly of the

**ADVANCED
SCIENCE NEWS**

www.advancedsciencenews.com

**ADVANCED
ENERGY
MATERIALS**

www.advenergymat.de

anatase phase and did not contain any carbon residues or impurity phases, as confirmed by XRD, Raman spectroscopy, TEM, TGA, and ICP-OES. The high oxygen activity applied upon calcination prevented the formation of Ti^{3+} defects. Instead, XPS and DFT studies suggested the formation of interstitial O''_i charge compensate for Nb^{5+} electron deficiency. The addition of small amounts of Nb resulted in the substitution of Ti^{4+} with isolated Nb^{5+} species causing an anisotropic lattice widening, as confirmed by XRD and DFT studies. DRS and PL revealed that these species introduced inter-bandgap states, which offer additional absorption sites in the visible region and facilitate charge recombination. In contrast, at high concentrations, Nb preferred to form clusters with shallow trap states within the CBM of TiO_2.

The performance of the gyroidal photocatalysts toward hydrogen evolution under both, UV and visible light conditions was among the highest reported in literature for pure TiO_2 photocatalysts. Interestingly, while the activity under UV light decreased by Nb doping due to the addition of charge recombination centers, the activity in the visible increased more than threefold upon the incorporation of 1 at% Nb. This enhancement was attributed to a more efficient absorption due to inter-bandgap sites. However, the activity dropped with increased Nb content, owing to the formation Nb clusters, which limited the absorption properties.

We further ascribe the superior activity of our gyroids to their beneficial porosity, large pore size, and 3D interconnectivity, which reduced kinetic limitations by pore diffusion, as well as to the compartmentalization of the narrow pore walls that allowed for short diffusion ways for photoexcited excitons. We believe that this unique pore architecture holds hitherto undiscovered optical benefits to photocatalysis, possibly related to the reported chiral and metamaterial-like behavior of the chiral alternating gyroid structure, which will stimulate further interest and future studies focusing on novel light–structure interactions.

4. Experimental Section

Materials: Benzene (99%, Alfa Aesar), THF (99%, <1000 ppm stabilizer, Alfa Aesar), chloroform ($CHCl_3$, 99,8+%, ACS, Alfa Aesar), methanol (99%, Alfa Aesar), *n*-butyllithium (*n*BuLi, 2.5 M in hexane, Alfa Aesar), *sec*-butyllithium (*sec*BuLi, 1.4 M in cyclohexane, Sigma Aldrich), 1,1-diphenylethylene (DPE, 98%, Alfa Aesar), isoprene (99%, <1000 ppm *p-tert*-butylcatechol, Sigma Aldrich), styrene (ReagentPlus, stabilized, Sigma Aldrich), ethylene oxide (EO, 99.8%, Praxair), calcium hydride (CaH_2, 1–20 mm granules, 88–98%, Alfa Aesar), potassium (98%, pieces in mineral oil, Fisher Scientific), naphthalene (99%, Fisher Scientific), titan(IV)isopropoxide (Ti(^{i}Prop)$_4$, 99.999%, Sigma Aldrich), niobium(V)ethoxide (Nb(OEt)$_5$, 99.95% trace metals basis, Sigma Aldrich), P25-TiO_2 (Aeroxide TiO_2 P25, Evonik), hydrochloric acid (HCl, reagent grade, 37%, Sigma Aldrich), and absolute tetrahydrofuran (THF$_{abs}$, 99.85%, extra dry, unstabilized, Acros Organics) were directly used as received or purified as described below.

Polymer Synthesis: The polymeric template ISO was synthesized via living sequential anionic polymerization.[56] In short, all chemicals were cleaned with either *n*BuLi (using DPE as indicator) or CaH_2 (stirred overnight). The synthesized poly(isoprene)-*block*-poly(styrene) was endcapped by double-distilled EO using benzene as solvent, and the lithium counter ion was exchanged by potassium. The PEO block was finally prepared in THF and the final ISO was precipitated from $CHCl_3$ in an aliquot of MeOH, filtrated, and further stored at 6 °C.

Synthesis of G^A-TiO2 and G^A-TNO1/3: The mesoporous TiO_2 samples were synthesized using EISA as already described in literature for related inorganic materials.[12a,c,21] In summary, a 4.5 mass% ISO in THF$_{abs}$ solution was combined with a certain amount of a precursor solution containing THF$_{abs}$, HCl, and Ti(^{i}Prop)$_4$ — for the preparation of TNO1/3 Nb(OEt)$_5$ partially replaces the Ti(^{i}Prop)$_4$. The mixture was stirred for 3 h at room temperature, transferred into 5 mL PTFE beakers and placed on a hotplate (35 °C) covered with a glass dome. After 24 h the rubber-like polymer/precursor disc was further aged under reduced atmosphere (90 °C/24 h) and calcined at 400 °C/3 h using a ramp of 1 °C min^{-1}.

Synthesis of NP-TiO2 and NP-TNO1/3: Nanoparticle references were prepared similar to their gyroidal counterparts, except there was no BCP present. Although no self-assembly was expected, the samples were placed in PTFE beakers on a hotplate under a glass dome, and further identically aged and calcined.

Material Characterization: The ISO polymer was characterized using combined proton nuclear magnetic resonance (^{1}H-NMR) and gel permeation chromatography (GPC). A sample of PI was taken during the preparation of ISO and analyzed on a Waters ambient-temperature GPC system equipped with a Waters 2410 differential RI detector. A concentration of 1 mg mL^{-1} was used and characterized using PSS PI standards. The final composition and molecular weight (M_W) were determined by normalizing the ^{1}H-NMR signals, measured on a Bruker Avance III HD Nanobay equipped with a SampleXpress autosampler and a BBFO probe for 5 mm tubes at 300 MHz, to the PI GPC results. The final polydispersity ($Đ_P$) was further analyzed by GPC.

The mesoporous structure was investigated using a high-resolution field emission SEM JSM 7500F from JEOL. The electron microscopy images were measured with an accelerating voltage of 1.0–1.5 kV on a gold-sputtered powdered sample placed on a carbon tape. TEM was carried out using a JEOL 2100F microscope. The powdered samples were dispersed in isopropanol, drop-casted on a copper grid with a lacey carbon film from Gatan and measured with an accelerating voltage of 200 kV.

TGA was used to determine the mass loss during calcination of the ISO/precursor hybrids and to search for residual carbon after successful template removal. A TG 209 F1 Libra system from Netzsch with an automatic sample changer was used and the samples were placed in alumina crucible. In a typical experiment, 10 mg of sample were heated in synthetic air with 20 °C min^{-1}.

XRD patterns were recorded on a Bruker Discover D8 powder diffraction unit, equipped with a Cu-Kα ($\lambda = 0.154$ nm) source, operating in reflection mode at 40 kV and 40 mA, using a sapphire single-crystal sample holder. Data were acquired using a Bruker area AXS detector VANTEC 500 (resolution: 2048 pixel). In the applied configuration, the angle subtended by the detector was 33° and integration was performed in a 2θ angle range between 16° and 100° with a step size of 0.02°.

SAXS measurements were performed on a Xenocs XEUSS 2.0 setup equipped with a Dectris Pilatus 1M detector and a Cu-kα source ($\lambda = 0.154$ nm). The sample-to-detector size was 2512 mm, calibrated with a silver behenate standard. Either a piece of the rubber-like polymer/precursor disc or a piece of the calcined, freestanding oxide sample was placed on a Kapton tape and measured without further modification. For 1D patterns, the primary beam was masked and total radial integration was performed. The scattering of pure Kapton tape was measured; no scattering was found in the q range of 0.02–0.08 Å^{-1}.

XPS measurements were carried out on a custom-built SPECS XPS spectrometer equipped with a monochromatized Al-Kα X-ray source (μFocus 350) and a hemispherical WAL-150 analyser (acceptance angle: 60°). All samples were mounted onto the sample holder using double-sided carbon tape. Pass energies of 100 and 30 eV and energy resolutions of 1 eV and 100 meV were used for survey and detail spectra, respectively (excitation energy: 1486.6 eV, beam energy and spot size: 70 W onto 400 μm, angle: 51° to sample surface normal, base pressure: 5×10^{-10} mbar, pressure during measurements: 2×10^{-9} mbar). Data analysis was performed using CASA XPS software, employing transmission corrections (as per the instrument vendor's specifications), Shirley/Tougaard backgrounds,[57] and Scofield sensitivity factors.[58] Charge

correction was applied so the adventitious carbon peak (C—C peak) was shifted to 284.8 BE. All content values shown are in units of relative atomic percent (at%), where the detection limit in survey measurements usually lies around 0.1–1 at%, depending on the element. The accuracy of XPS measurements is around 10–20% of the values shown. Assignment of different components was primarily done using ref. [59].

Raman spectra (RAMAN) were measured with a LabRAM Aramis from Horiba Jobin Yvon, using a 633 nm helium-neon laser with an 1800 gr mm^{-1} grating (0.75 cm^{-1} pixel^{-1}) in a range from 50 to 1000 cm^{-1}. The acquisition time was 10 s with a fourfold accumulation. Calibration was done with a Si wafer and TiO$_2$ spectra were normalized in intensity to either E$_g$ (144 cm^{-1}) or combined mode of B$_{1g}$/A$_{1g}$ (centered at 514 cm^{-1}) for full spectra or zoomed inset, respectively.

A Quantachrome Autosorb-6B was used for nitrogen gas sorption. Samples were degassed at 100 °C for 3 d and a total of 19 points for the adsorption and the desorption, respectively, were collected. The BET equation[60] was applied for the calculation of the specific surface area (SSA$_{BET}$).

DRS was measured on an Agilent Cary 5000 UV–visible–NIR high-performance spectrophotometer, equipped with an Agilent diffuse reflectance accessory (DRAs). Powdered samples were filled in a sample holder and measured through a quartz window with an acquisition time of 0.1 s with a resolution of 1 nm (scan rate: 600 nm min^{-1}). Calibration was done with 100% reflectance PTFE reference plate and a zero-reflectance background by blocking the beam.

For the fluorescence spectroscopic (PL) measurements, an Edinburgh Instruments FPS920 photoluminescence spectroscopy setup was used. This setup contains a XE900 Xenon Arc Lamp (500 W) as an illumination source, double Czerny–Turner monochromators (type TMS300) at both excitation and emission arms as well as a S900 single-photon photomultiplier (type R928) as the detector. In a single measurement, a powdered photocatalyst was squeezed between two quartz plates and put into the excitation light beam, while the reflected light was measured. UV and visible light excitation wavelengths were set to 350 ± 5 and 420 ± 5 nm, respectively. The signal was acquired in the range between 400 and 800 nm. To filter out excitation wavelength, cutoff filters of 395 and 455 nm were used for UV and visible excitations, respectively.

In order to support some of the experimental results and their interpretation, DFT calculations on the electronic structure of Nb impurities in Anatase using the WIEN2k code were performed.[61] The calculations employed the generalized gradient approximation[62] and a Hubbard-U term[63] with an U value of 7 eV. It was shown earlier[64] that U values above ≈5 eV lead to localization of Ti-3d electrons and a spin-polarized solution can be found; a larger U value also leads to a more credible bandgap of anatase.[65] To simulate the impurities, $4 \times 4 \times 2$ face-centered supercells (96 atoms/cell) were employed and convergence with body-centered cells (192 atoms/cell) was verified. The results for a single Nb impurity are similar to previous reports in literature.[26d,64-66]

Photocatalytic H$_2$ evolution was quantified in a closed home-built flow reactor, which was top-irradiated with a 200 W super pressure Hg lamp (UV: λ = 220–400 nm, visible: λ = 400–700 nm, Lumatec). During the reaction, the reactor was constantly purged with argon 5.0 as a carrier gas (flow rate: 30 mL min^{-1}, controlled with a mass flow controller, MCC Instruments). The amounts of generated hydrogen in the flow were quantified by a gas analyzer (X-Stream, Emerson) equipped with a thermal conductivity detector (TCD). 10 mg of each powdered photocatalyst were dispersed in a 10 mL aqueous methanol solution (50 vol%) by ultrasonication for 1 min. The reaction mixture was degassed by bubbling argon for 5 min and a certain amount of an aqueous H$_2$PtCl$_6$ solution was added to the mixture before closing the top lid to allow for in situ photodeposition of 0.5 mass% of platinum nanoparticles used as a cocatalyst.

Supporting Information

Supporting Information is available from the Wiley Online Library or from the author.

Conflict of Interest

The authors declare no conflict of interest.

[1] a) A. Fujishima, K. Honda, *Nature* **1972**, *238*, 37; b) A. Kudo, Y. Miseki, *Chem. Soc. Rev.* **2009**, *38*, 253; c) K. Maeda, K. Domen, *J. Phys. Chem. Lett.* **2010**, *1*, 2655.

[2] K. Hashimoto, H. Irie, A. Fujishima, *Jpn. J. Appl. Phys.* **2005**, *44*, 8269.

[3] K. Maeda, K. Domen, *Bull. Chem. Soc. Jpn.* **2016**, *89*, 627.

[4] a) S. J. A. Moniz, S. A. Shevlin, D. J. Martin, Z.-X. Guo, J. Tang, *Energy Environ. Sci.* **2015**, *8*, 731; b) J. Ran, J. Zhang, J. Yu, M. Jaroniec, S. Z. Qiao, *Chem. Soc. Rev.* **2014**, *43*, 7787; c) X. Zou, Y. Zhang, *Chem. Soc. Rev.* **2015**, *44*, 5148.

[5] a) F. Bosc, A. Ayral, P. A. Albouy, C. Guizard, *Chem. Mater.* **2003**, *15*, 2463; b) J. Zhang, Q. Xu, Z. Feng, M. Li, C. Li, *Angew. Chem., Int. Ed.* **2008**, *47*, 1766; c) E. Baldini, L. Chiodo, A. Dominguez, M. Palummo, S. Moser, M. Yazdi-Rizi, G. Auböck, B. P. P. Mallett, H. Berger, A. Magrez, C. Bernhard, M. Grioni, A. Rubio, M. Chergui, *Nat. Commun.* **2017**, *8*, 13.

[6] a) L. D. Li, J. Q. Yan, T. Wang, Z. J. Zhao, J. Zhang, J. L. Gong, N. J. Guan, *Nat. Commun.* **2015**, *6*, 5881; b) A.-W. Xu, Y. Gao, H.-Q. Liu, *J. Catal.* **2002**, *207*, 151.

[7] a) N. Bouazza, M. Ouzzine, M. A. Lillo-Rodenas, D. Eder, A. Linares-Solano, *Appl. Catal., B* **2009**, *92*, 377; b) D. Eder, *Chem. Rev.* **2010**, *110*, 1348.

[8] L. Miao, S. Tanemura, S. Toh, K. Kaneko, M. Tanemura, *Appl. Surf. Sci.* **2004**, *238*, 175.

[9] J. Yu, L. Qi, M. Jaroniec, *J. Phys. Chem. C* **2010**, *114*, 13118.

[10] a) G. Wang, H. Wang, Y. Ling, Y. Tang, X. Yang, R. C. Fitzmorris, C. Wang, J. Z. Zhang, Y. Li, *Nano Lett.* **2011**, *11*, 3026; b) H. B. Wu, H. H. Hng, X. W. Lou, *Adv. Mater.* **2012**, *24*, 2567.

[11] a) Y. Noda, B. Lee, K. Domen, J. N. Kondo, *Chem. Mater.* **2008**, *20*, 5361; b) Y. Takahara, J. N. Kondo, T. Takata, D. Lu, K. Domen, *Chem. Mater.* **2001**, *13*, 1194.

[12] a) M. Stefik, S. Guldin, S. Vignolini, U. Wiesner, U. Steiner, *Chem. Soc. Rev.* **2015**, *44*, 5076; b) J. G. Werner, T. N. Hoheisel, U. Wiesner, *ACS Nano* **2014**, *8*, 731; c) S. W. Robbins, P. A. Beaucage, H. Sai, K. W. Tan, J. G. Werner, J. P. Sethna, F. J. DiSalvo, S. M. Gruner, R. B. Van Dover, U. Wiesner, *Sci. Adv.* **2016**, *2*, e1501119; d) Z. Wei, S. Fanfei, P. Kai, T. Guohui, J. Baojiang, R. Zhiyu, T. Chungui, F. Honggang, *Adv. Funct. Mater.* **2011**, *21*, 4193; e) A. Cherevan, L. Deilmann, T. Weller, D. Eder, R. Marschall, *ACS Appl. Energy Mater.*, https://doi.org/10.1021/acsaem.8b01123.

[13] a) T. S. Dörr, A. Pelz, P. Zhang, T. Kraus, M. Winter, H.-D. Wiemhöfer, *Chem. - Eur. J.* **2018**, *24*, 8061; b) J. G. Werner, G. G. Rodriguez-Calero, H. D. Abruna, U. Wiesner, *Energy Environ. Sci.* **2018**, *11*, 1261.

[14] a) R. Liu, Y. Ren, Y. Shi, F. Zhang, L. Zhang, B. Tu, D. Zhao, *Chem. Mater.* **2008**, *20*, 1140; b) T. Weller, J. Sann, R. Marschall, *Adv. Energy Mater.* **2016**, *6*, 1600208.

[15] L. Li, M. Krissanasaeranee, S. W. Pattinson, M. Stefik, U. Wiesner, U. Steiner, D. Eder, *Chem. Commun.* **2010**, *46*, 7620.

[16] T. S. Dörr, S. Fleischmann, M. Zeiger, I. Grobelsek, P. W. de Oliveira, V. Presser, *Chem. - Eur. J.* **2018**, *24*, 6358.

[17] T. Weller, L. Deilmann, J. Timm, T. S. Dörr, P. A. Beaucage, A. S. Cherevan, U. B. Wiesner, D. Eder, R. Marschall, *Nanoscale* **2018**, *10*, 3225.

[18] M. Templin, A. Franck, A. Du Chesne, H. Leist, Y. Zhang, R. Ulrich, V. Schädler, U. Wiesner, *Science* **1997**, *278*, 1795.

[19] D. Zhao, J. Feng, Q. Huo, N. Melosh, G. H. Fredrickson, B. F. Chmelka, G. D. Stucky, *Science* **1998**, *279*, 548.

[20] P. Docampo, M. Stefik, S. Guldin, R. Gunning, N. A. Yufa, N. Cai, P. Wang, U. Steiner, U. Wiesner, H. J. Snaith, *Adv. Energy Mater.* **2012**, *2*, 676.

[21] A. S. Cherevan, S. Robbins, D. Dieterle, P. Gebhardt, U. Wiesner, D. Eder, *Nanoscale* **2016**, *8*, 16694.

[22] S. Guldin, S. Huttner, P. Tiwana, M. C. Orilall, B. Ulgut, M. Stefik, P. Docampo, M. Kolle, G. Divitini, C. Ducati, S. A. T. Redfern, H. J. Snaith, U. Wiesner, D. Eder, U. Steiner, *Energy Environ. Sci.* **2011**, *4*, 225.

[23] a) T. Dittrich, *Phys. Status Solidi A* **2000**, *182*, 447; b) T. Dittrich, J. Weidmann, F. Koch, I. Uhlendorf, I. Lauermann, *Appl. Phys. Lett.* **1999**, *75*, 3980.

[24] K. Lalitha, G. Sadanandam, V. D. Kumari, M. Subrahmanyam, B. Sreedhar, N. Y. Hebalkar, *J. Phys. Chem. C* **2010**, *114*, 22181.

[25] A. Kubacka, G. Colon, M. Fernandez-Garcia, *Catal. Today* **2009**, *143*, 286.

[26] a) D. D. Mulmi, T. Sekiya, N. Kamiya, S. Kurita, Y. Murakami, T. Kodaira, *J. Phys. Chem. Solids* **2004**, *65*, 1181; b) L. R. Sheppard, T. Bak, J. Nowotny, *J. Phys. Chem. B* **2006**, *110*, 22447; c) M. Valigi, D. Cordischi, G. Minelli, P. Natale, P. Porta, C. P. Keijzers, *J. Solid State Chem.* **1988**, *77*, 255; d) H.-Y. Lee, J. Robertson, *J. Appl. Phys.* **2013**, *113*, 213706.

[27] L. N. Kong, C. H. Wang, H. Zheng, X. T. Zhang, Y. C. Liu, *J. Phys. Chem. C* **2015**, *119*, 16623.

[28] T. Nikolay, L. Larina, O. Shevaleevskiy, B. T. Ahn, *Energy Environ. Sci.* **2011**, *4*, 1480.

[29] M. C. Orilall, U. Wiesner, *Chem. Soc. Rev.* **2011**, *40*, 520.

[30] Y. Qiu, F. Ouyang, R. Zhu, *Int. J. Hydrogen Energy* **2017**, *42*, 11364.

[31] W. F. Zhang, Y. L. He, M. S. Zhang, Z. Yin, Q. Chen, *J. Phys. D: Appl. Phys.* **2000**, *33*, 912.

[32] A. M. Ruiz, G. Dezanneau, J. Arbiol, A. Cornet, J. R. Morante, *Chem. Mater.* **2004**, *16*, 862.

[33] M. Thommes, K. Kaneko, A. V. Neimark, J. P. Olivier, F. Rodriguez-Reinoso, J. Rouquerol, K. S. Sing, *Pure Appl. Chem.* **2015**, *87*, 1051.

[34] T. H. Epps, E. W. Cochran, C. M. Hardy, T. S. Bailey, R. S. Waletzko, F. S. Bates, *Macromolecules* **2004**, *37*, 7085.

[35] A. J. Gardecka, G. K. L. Goh, G. Sankar, I. P. Parkin, *J. Mater. Chem. A* **2015**, *3*, 17755.

[36] P. Le Fèvre, J. Danger, H. Magnan, D. Chandesris, J. Jupille, S. Bourgeois, M. A. Arrio, R. Gotter, A. Verdini, A. Morgante, *Phys. Rev. B* **2004**, *69*, 155421.

[37] a) M. Z. Atashbar, H. T. Sun, B. Gong, W. Wlodarski, R. Lamb, *Thin Solid Films* **1998**, *326*, 238; b) M. Kim, C. Kwon, K. Eom, J. Kim, E. Cho, *Sci. Rep.* **2017**, *7*, 44411.

[38] J. Wang, X. Wang, Z. Cui, B. Liu, M. Cao, *Phys. Chem. Chem. Phys.* **2015**, *17*, 14185.

[39] T. M. Breault, B. M. Bartlett, *J. Phys. Chem. C* **2012**, *116*, 5986.

[40] F. Zuo, L. Wang, T. Wu, Z. Zhang, D. Borchardt, P. Feng, *J. Am. Chem. Soc.* **2010**, *132*, 11856.

[41] a) J. Yang, X. Zhang, C. Wang, P. Sun, L. Wang, B. Xia, Y. Liu, *Solid State Sci.* **2012**, *14*, 139; b) B.-X. Chen, H.-S. Rao, W.-G. Li, Y.-F. Xu, H.-Y. Chen, D.-B. Kuang, C.-Y. Su, *J. Mater. Chem. A* **2016**, *4*, 5647.

[42] B. Roose, K. C. Gödel, S. Pathak, A. Sadhanala, J. P. C. Baena, B. D. Wilts, H. J. Snaith, U. Wiesner, M. Grätzel, U. Steiner, A. Abate, *Adv. Energy Mater.* **2016**, *6*, 1501868.

[43] M. S. J. Marshall, D. T. Newell, D. J. Payne, R. G. Egdell, M. R. Castell, *Phys. Rev. B* **2011**, *83*, 035410.

[44] Y. D. Wang, B. M. Smarsly, I. Djerdj, *Chem. Mater.* **2010**, *22*, 6624.

[45] H. Xu, P. Reunchan, S. Ouyang, H. Tong, N. Umezawa, T. Kako, J. Ye, *Chem. Mater.* **2013**, *25*, 405.

[46] F. Amano, M. Nakata, A. Yamamoto, T. Tanaka, *Catal. Sci. Technol.* **2016**, *6*, 5693.

[47] A. L. Luna, D. Dragoe, K. Wang, P. Beaunier, E. Kowalska, B. Ohtani, D. B. Uribe, M. A. Valenzuela, H. Remita, C. Colbeau-Justin, *J. Phys. Chem. C* **2017**, *121*, 14302.

[48] T. Sreethawong, S. Yoshikawa, *Catal. Commun.* **2005**, *6*, 661.

[49] Z. Lian, W. Wang, G. Li, F. Tian, K. S. Schanze, H. Li, *ACS Appl. Mater. Interfaces* **2017**, *9*, 16959.

[50] K. Yamaguti, S. Sato, *J. Chem. Soc., Faraday Trans. 1* **1985**, *81*, 1237.

[51] W. Zhou, W. Li, J.-Q. Wang, Y. Qu, Y. Yang, Y. Xie, K. Zhang, L. Wang, H. Fu, D. Zhao, *J. Am. Chem. Soc.* **2014**, *136*, 9280.

[52] K. Hur, Y. Francescato, V. Giannini, S. A. Maier, R. G. Hennig, U. Wiesner, *Angew. Chem., Int. Ed.* **2011**, *50*, 11985.

[53] S. Vignolini, N. A. Yufa, P. S. Cunha, S. Guldin, I. Rushkin, M. Stefik, K. Hur, U. Wiesner, J. J. Baumberg, U. Steiner, *Adv. Mater.* **2012**, *24*, OP23.

[54] G. M. Haselmann, D. Eder, *ACS Catal.* **2017**, *7*, 4668.

[55] M. L. Sauer, D. F. Ollis, *J. Catal.* **1996**, *163*, 215.

[56] a) M. A. Hillmyer, F. S. Bates, *Macromolecules* **1996**, *29*, 6994; b) J. Chatterjee, S. Jain, F. S. Bates, *Macromolecules* **2007**, *40*, 2882.

[57] a) S. Tougaard, *Surf. Interface Anal.* **1997**, *25*, 137; b) D. A. Shirley, *Phys. Rev. B* **1972**, *5*, 4709.

[58] J. H. Scofield, *J. Electron Spectrosc. Relat. Phenom.* **1976**, *8*, 129.

[59] a) C. D. Wagner, A. V. Naumkin, A. Kraut-Vass, J. W. Allison, C. J. Powell, J. R. Rumble, *NIST X-ray Photoelectron Spectroscopy Database, NIST Standard Reference Database Number 20,* National Institute of Standards and Technology, Gaithersburg, MD **2000**; b) G. Beamson, D. Briggs, *High Resolution XPS of Organic Polymers: The Scienta ESCA300 Database*, Wiley, New York **1992**.

[60] S. Brunauer, P. H. Emmett, E. Teller, *J. Am. Chem. Soc.* **1938**, *60*, 309.

[61] P. Blaha, K. Schwarz, G. K. H. Madsen, D. Kvasnicka, J. Luitz, R. Laskowski, F. Tran, L. D. Marks, *WIEN2k, An Augmentented Plane Wave + Local Orbitals Program for Calculating Crystal Properties*, Karlheinz Schwarz, Vienna University of Technology, Vienna, Austria **2018**.

[62] J. P. Perdew, K. Burke, M. Ernzerhof, *Phys. Rev. Lett.* **1996**, *77*, 3865.

[63] S. L. Dudarev, G. A. Botton, S. Y. Savrasov, C. J. Humphreys, A. P. Sutton, *Phys. Rev. B* **1998**, *57*, 1505.

[64] Y. Kesong, D. Ying, H. Baibiao, F. Yuan Ping, *J. Phys. D: Appl. Phys.* **2014**, *47*, 275101.

[65] X. Han, K. Song, L. Lu, Q. Deng, X. Xia, G. Shao, *J. Mater. Chem. C* **2013**, *1*, 3736.

[66] a) B. J. Morgan, D. O. Scanlon, G. W. Watson, *J. Mater. Chem.* **2009**, *19*, 5175; b) S. Khan, H. Cho, D. Kim, S. S. Han, K. H. Lee, S.-H. Cho, T. Song, H. Choi, *Appl. Catal., B* **2017**, *206*, 520.